Communication

A Multiplicative Regularizer Augmented with Spatial Priors for Microwave Imaging

Nozhan Bayat, *Student, IEEE* and Puyan Mojabi, *Member, IEEE*

***Abstract*—The standard weighted L_2 norm total variation multiplicative regularization (MR) term originally developed for microwave imaging algorithms is modified to take into account structural prior information, also known as spatial priors (SP), about the object being imaged. This modification adds one extra term to the integrand of the standard MR, thus, being referred to as an augmented MR (AMR). The main advantage of the proposed approach is that it requires a minimal change to the existing microwave imaging algorithms that are already equipped with the MR. Using two experimental data sets, it is shown that the proposed AMR (i) can handle partial SP, and (ii) can, to some extent, enhance the quantitative accuracy achievable from microwave imaging.**

***Index Terms*—Microwave imaging, regularization, spatial priors (SP), inversion.**

I. Introduction

MICROWAVE imaging is a non-invasive imaging method with which quantitative images of the relative complex permittivity profiles of the objects of interest (OI) can be created. This is often done by applying an electromagnetic inverse scattering algorithm (or, simply an inversion algorithm hereafter) to the microwave scattered field data collected outside the OI. Through an iterative process, the inversion algorithm reconstructs a quantitative image of the OI's relative complex permittivity profile. In some situations, the measured data might not have sufficient information content to reconstruct the OI to the desired accuracy. In such cases, one option is to provide the inversion algorithm with some prior information about the OI. To understand this better, let us consider a simple geometrical example. Assume that we would like to get to the point $(2, 3, 4)$ from the origin but we only have access to $\hat{x}$ and $\hat{y}$ (i.e., the unit vectors along the x and y axes); it is then obvious that we can never get to this point. However, if $\hat{z}$ is added to our basis vectors, we are then able to get to the desired point. This is, to some extent, parallel to MWI: the measured scattered data affect the basis vectors forming a subspace in which the unknown reconstructed complex permittivity profile has to lie. If the measured data do not yield all the basis vectors required to achieve the desired image accuracy, the injection of prior information about the OI might be able to provide the inversion algorithm with a new set of basis vectors with which enhanced reconstruction can be potentially achieved.

This Communication is focused on a method to inject prior spatial information about the OI, also known as prior structural information or simply spatial priors (SP), into the inversion algorithm. (These SP may come from a different higher-resolution imaging modality such as magnetic resonance imaging [1].) Incorporation of SP into the inversion algorithm has already been considered by several authors using different approaches [1]–[11]. These methods can be classified (at least) under three categories: (i) those that favour similarity of the reconstructed permittivity values in each region within the SP, e.g., [4], (ii) those that use an inhomogeneous background medium derived from the SP for the inversion algorithm, e.g., [9], and (iii) those that use special basis functions obtained based on the SP for the expansion of the unknown permittivity profile in the inversion process, e.g., [8]. The proposed algorithm in this paper enforces SP in a different manner: via providing *edge* information for the inversion algorithm based on the SP. (Note that an edge represents the transition from one region to another in the complex permittivity image.)

The main feature of this algorithm is that it only requires a *minimal* change to the existing Gauss-Newton inversion (GNI) and contrast source inversion (CSI) algorithms equipped with the standard multiplicative regularizer (MR). (The term 'standard' indicates the common MR used in the literature: the weighted L_2 norm total variation multiplicative regularizer, e.g., see [12].) Using the proposed SP technique, the existing MR-GNI and MR-CSI algorithms can be easily changed to accommodate the available SP by augmenting the integrand of the standard MR by an extra term. Thus, we refer to it as an augmented MR (AMR). When the proposed AMR is used with GNI and CSI, we refer to the resulting algorithms as AMR-GNI and AMR-CSI respectively. In this Communication, we first briefly review the standard MR, and then describe the small change that needs to be done in order to incorporate SP into the existing MR. We then evaluate the performance of AMR-GNI and AMR-CSI against two experimental data sets for two-dimensional scalar microwave imaging. In addition, we compare the performance of the proposed algorithms against an existing SP algorithm recently developed by the authors. This algorithm, denoted by MRSP-GNI [10], belongs to the class of SP algorithms in which the *similarity* between the reconstructed relative permittivity in each region within the SP is favoured by the algorithm. That is in contrast to the AMR-GNI and AMR-CSI algorithms in which the SP are injected in the form of favoured *edges* in the imaging domain.

This paragraph of the first footnote will contain the date on which you submitted your paper for review. The authors acknowledge Natural Sciences and Engineering Research Council (NSERC) of Canada, and Canada Research Chair Program for their financial support.

The authors are with the Department of Electrical and Computer Engineering at the University of Manitoba, Winnipeg, MB, Canada (email: Puyan.Mojabi@UManitoba.ca).

II. Multiplicative Regularizer (MR) - Review

The MR-GNI and MR-CSI algorithms use the following multiplicative regularization term [12]

$$\mathcal{C}_n^{\text{MR}}(\chi) = \frac{1}{A}\int_D \frac{|\nabla\chi(\mathbf{r})|^2 + \delta_n^2}{|\nabla\chi_n(\mathbf{r})|^2 + \delta_n^2} d\mathbf{s} \tag{1}$$

to regularize their associated cost functionals at the nth iteration of the their iterative algorithms. In (1), A is the area of the imaging domain D, χ is the unknown relative complex permittivity contrast profile, χ_n is the known estimate of χ at the nth iteration, $\mathbf{r}$ is the position vector spanning the imaging domain, ∇ is the gradient operator, and $|\cdot|$ is the magnitude operator. The steering parameter δ_n^2, which is a real number, gets smaller as the inversion algorithm gets closer to the final solution. (For the expressions of δ_n^2 in the MR-GNI and MR-CSI algorithms, see [13] and [12], respectively.) The operation of MR has been described in previous works such as [12], [14], [15]; herein, we only provide a quick overview. To this end, let us consider the gradient of the MR at the nth iteration for a given χ [16, Appendix D.3]

$$\mathcal{L}_n^{\text{MR}}(\chi) = -\nabla\cdot(b_n^2(\mathbf{r})\nabla\chi) \tag{2}$$

where '$\nabla\cdot$' is the divergence operator, and $b_n^2(\mathbf{r})$ is an inhomogeneous weight given as

$$b_n^2(\mathbf{r}) = \frac{1}{A}\frac{1}{|\nabla\chi_n(\mathbf{r})|^2 + \delta_n^2}. \tag{3}$$

In early iterations, δ_n^2 is dominant as compared to $|\nabla\chi_n(\mathbf{r})|^2$. Therefore, in early iterations, $b_n^2(\mathbf{r})$ can be approximated by the constant number $1/(A\delta_n^2)$. Consequently, in early iterations, $\mathcal{L}_n^{\text{MR}}$ operator can be approximated by

$$\mathcal{L}_n^{\text{MR}}(\chi) \overset{\text{Early iterations}}{\approx} \frac{1}{A\delta_n^2}\nabla\cdot(\nabla\chi) = \frac{1}{A\delta_n^2}\nabla^2\chi \tag{4}$$

where '∇^2' is the Laplacian operator. That is, in early iterations, MR works similar to Laplacian regularization which aims to smoothen the reconstruction. After early iterations, the relative magnitude of $|\nabla\chi_n(\mathbf{r})|^2$ and δ_n^2 should be considered locally in the imaging domain. If in a region within the imaging domain, δ_n^2 is dominant compared to $|\nabla\chi_n(\mathbf{r})|^2$, the above Laplacian approximation is still valid locally, and the regularization operator then attempts to smooth out that region. Otherwise, it favours to reconstruct an edge in that region.

III. Augmented Multiplicative Regularizer (AMR)

Let us now consider that we have some available SP about the OI. Given the SP, we can then guide the inversion algorithm regarding the locations at which some edges (i.e., the boundaries between different regions) are to be expected. To this end, we not only rely on the relative magnitude of $|\nabla\chi_n(\mathbf{r})|^2$ and δ_n^2 for edge detection as in (1), but we also introduce an extra term based on the available SP to further guide the inversion algorithm in edge detection. Thus, we modify the MR given in (1) to an augmented MR (or, simply AMR) as follows

$$\mathcal{C}_n^{\text{AMR}}(\chi) = \frac{1}{A}\int_D \frac{|\nabla\chi(\mathbf{r})|^2 + Q^2|\nabla P(\mathbf{r})|^2 + \delta_n^2}{|\nabla\chi_n(\mathbf{r})|^2 + Q^2|\nabla P(\mathbf{r})|^2 + \delta_n^2} d\mathbf{s}. \tag{5}$$

As can be seen from (5), we have now augmented the integrand of the MR with an extra term, $Q^2|\nabla P(\mathbf{r})|^2$, where P incorporates SP. In our implementation, P is a matrix containing some numbers, each of which represents an expected region within the imaging domain D. For example, if the SP contain four regions, we assign the values of 1, 0.75, 0.50, and 0.25 to each of these regions.[1] In addition, Q is a scaling factor that controls the relative weight of $|\nabla P|^2$. In all the examples shown in this Communication, this scaling factor has been set to $Q = 1$.

One question that may arise is the following: *why do we use both $|\nabla\chi_n(\mathbf{r})|^2$ and $|\nabla P(\mathbf{r})|^2$ in the AMR?* The main reason lies in the fact that if the SP only provide *partial* structural information, the presence of $|\nabla\chi_n(\mathbf{r})|^2$ may still enable the inversion algorithm to retrieve the edges that are not present in the SP. In addition, if some of the edges provided by the SP are wrong, the presence of $|\nabla\chi_n(\mathbf{r})|^2$ may alleviate the effects of the wrong edges to some extent. These will be observed in the next section.

Similar to the MR, the gradient of the AMR at the nth iteration for a given χ will become

$$\mathcal{L}_n^{\text{AMR}}(\chi) = -\nabla\cdot(a_n^2(\mathbf{r})\nabla\chi) \tag{6}$$

where

$$a_n^2(\mathbf{r}) = \frac{1}{A}\frac{1}{|\nabla\chi_n(\mathbf{r})|^2 + Q^2|\nabla P(\mathbf{r})|^2 + \delta_n^2}. \tag{7}$$

In early iterations, since χ_n is small[2], $|\nabla P(\mathbf{r})|^2$ will be dominant, and therefore, the inversion algorithm tries to favour the edges within P. As the algorithms gets closer to the true solution, it is both $|\nabla\chi_n(\mathbf{r})|^2$ and $|\nabla P(\mathbf{r})|^2$ (in conjunction with δ_n^2) that together affect the enforcement of the reconstructed edges within the imaging domain. Finally, we would like to note the simplicity of incorporating SP within the existing MR-GNI and MR-CSI algorithms. Herein, the only modification performed was to replace b_n^2 given in (3) by a_n^2 given in (7). Upon this replacement, the two algorithms are referred to as AMR-GNI and AMR-CSI.

IV. Experimental Results

We consider two previously-reported experimental data sets to evaluate the performance of the AMR-GNI and AMR-CSI algorithms. The first data set is the so-called *FoamTwinDielTM* data set [17] collected by the Fresnel Institute in an anechoic chamber. The second data set was collected by the Electromagnetic Imaging Laboratory at the University of Manitoba from a human forearm [13] in the matching fluid of salt water. In all the cases presented below, all the inversion algorithms start with a *trivial* initial guess, which is the zero contrast for the AMR-GNI algorithm, and the back-propagated solution for the AMR-CSI algorithm.

[1] As another example, if the SP have two regions, we assign the values of 1 and 0.5 to each of these regions in the matrix P. Since a typical maximum contrast value in microwave imaging (assuming the presence of a matching medium) is about one, we have set the maximum value for the elements of P to unity in an attempt to make $|\nabla\chi_n(\mathbf{r})|^2$ and $|\nabla P(\mathbf{r})|^2$ relatively balanced in (5).

[2] For example, the MR-GNI algorithm starts with a zero initial guess, so, in the first iteration χ is zero, and therefore, its gradient is zero as well.

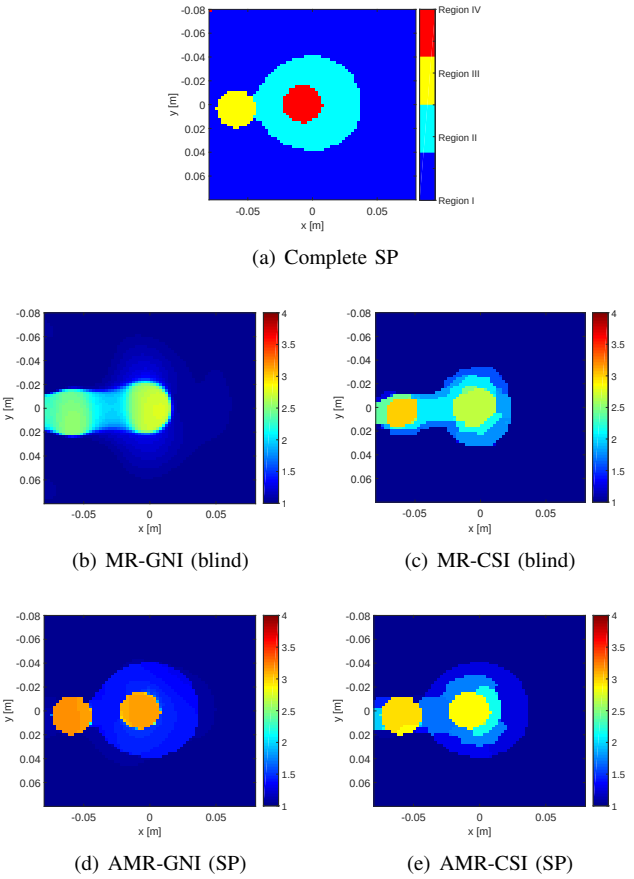

(a) Complete SP

(b) MR-GNI (blind)

(c) MR-CSI (blind)

(d) AMR-GNI (SP)

(e) AMR-CSI (SP)

Fig. 1. (a) The SP showing four regions of the *FoamTwinDielTM* target of Institut Fresnel. The reconstructed real part of the relative complex permittivity at 2 GHz using (b) MR-GNI, (c) MR-CSI, (d) AMR-GNI, and (e) AMR-CSI.

A. FoamTwinDielTM Data Set

This target consists of three dielectric cylinders two of which have a diameter of 31 mm, and a relative permittivity of $\epsilon_r = 3 \pm 0.3$ and the other one has a diameter of 80 mm and a relative permittivity of 1.45 ± 0.15. The geometry of this target can be found in [17]. Herein, we have set the size of the imaging domain to 16×16 cm^2 discretized into 70×70 square cells. This target was illuminated from 18 different angles, and the resulting scattered field are collected at 241 data points per transmitter. (This procedure has been repeated at 9 different operational frequencies ranging form 2 GHz to 10 GHz with 1 GHz increment.) Similar to the procedure outlined in [18], we have created the SP shown in Figure 1(a) for this target.

Let us now consider the inversion at the *lowest* frequency of operation, i.e., 2 GHz. The reason for this intentional choice of this frequency is for the *blind*[3] inversion using MR-GNI and MR-CSI to not yield sufficient resolution; see Figure 1(b)-(c). (These blind reconstructions have already been shown by several groups including the authors, e.g., [18], and are only presented herein for the sake of side-by-side comparison with the inversion using the SP.) Incorporating the SP into the inversion algorithms results in the AMR-GNI and AMR-CSI reconstructions shown in Figure 1(d)-(e). As can be seen, the AMR-GNI almost perfectly reconstructs the relative permittivities of the dielectric objects. In addition, the AMR-CSI reconstructed values, although not perfect, are still better than those obtained by MR-CSI. Moreover, we have also inverted the 2 GHz data set with a similar SP using the MRSP-GNI algorithm, see [18]. Since the MRSP-GNI algorithm provided a reconstruction very similar to the AMR-GNI algorithm, it is not shown here for brevity. In the next step, we only provide *partial* SP to the inversion algorithms. The partial SP are illustrated in Figure 2(a) where it is clear that the SP have no knowledge of the inner dielectric cylinder. The reconstruction results of the MRSP-GNI, AMR-GNI, and AMR-CSI are shown in Figures 2(b)-(d). As can be seen, the MRSP-GNI algorithm was not capable of retrieving the inner dielectric cylinder as it was misguided by the partial SP.[4] However, both AMR-GNI and AMR-CSI are successful in the detection of a smaller dielectric cylinder within the larger one.

[3]The term *blind* inversion indicates that no prior information has been used in the inversion process.

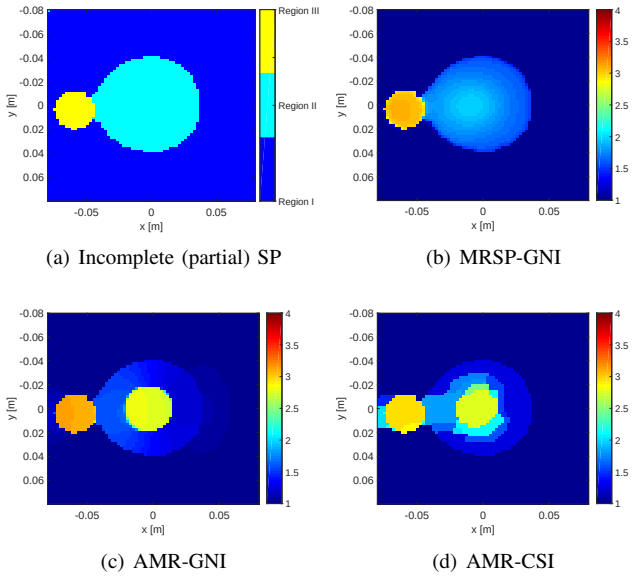

(a) Incomplete (partial) SP

(b) MRSP-GNI

(c) AMR-GNI

(d) AMR-CSI

Fig. 2. (a) The incomplete (partial) SP showing three regions within the imaging domain with the inner cylinder missing from the SP. The reconstructed real part of the relative complex permittivity at 2 GHz using (b) MRSP-GNI, (c) AMR-GNI and (d) AMR-CSI.

B. Forearm Data Set

This data set [13], [19] was collected from a human forearm at 0.8 GHz using 24 co-resident dipole antennas immersed in a matching fluid (salt water) with the relative complex permittivity of about $77 - j17$. The blind inversion of this data set, which was originally reported in [13], [19], are

[4]It should be noted that MRSP-GNI is, in fact, able to retrieve the inner cylinder *if* it is told that the available SP is only partial and is not accurate within the larger cylinder. As discussed in [10], the mechanism with which we can tell the MRSP-GNI algorithm that a given SP is partial is via the use of a probability vector. Herein, we have not used this probability vector. Subsequently, MRSP-GNI favours similar permittivity values within Region II of Figure 2(a), thus, missing the inner cylinder. On the other hand, in [18], the MRSP-GNI algorithm was told that the SP within Region II is not accurate, thus, we were able to reconstruct the inner cylinder using MRSP-GNI.

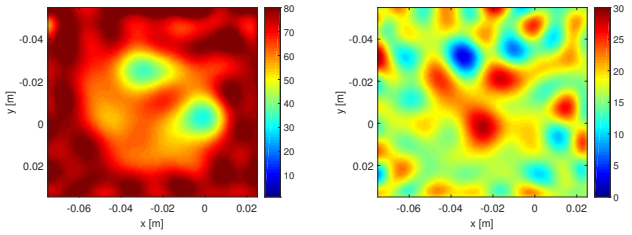

(a) $\mathrm{Re}(\epsilon_r)$, MR-GNI (b) $-\mathrm{Im}(\epsilon_r)$, MR-GNI

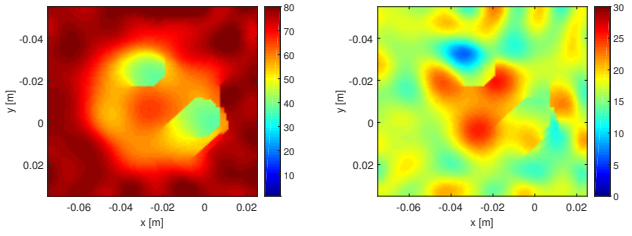

(c) $\mathrm{Re}(\epsilon_r)$, MR-CSI (d) $-\mathrm{Im}(\epsilon_r)$, MR-CSI

Fig. 3. Blind inversion of the human forearm data at 0.8 GHz using the (a)-(b) MR-GNI algorithm and (c)-(d) MR-CSI algorithm. (Left and right columns represent the real and imaginary parts of the reconstructed relative complex permittivity respectively.)

presented in Figure 3 for the sake of comparison with inversion using SP.[5] (The imaging domain has the size of 10×9 cm^2 discretized to 100×100 cells.) One item to note in the blind inversions is the fact that although the presence of the two bones are clear, their reconstructed relative permittivities are over-estimated. (According to [13], the relative complex permittivities of the bone and muscle are expected to be about $13 - j3$ and $56 - j20$ at the frequency of operation.)

In the next step, we utilize the image from the magnetic resonance imaging (MRI) of the forearm shown in Figure 4(a) to create the SP shown in Figure 4(b).[6] The reconstruction of the real and imaginary parts of the relative complex permittivity using the SP by the MRSP-GNI, AMR-GNI, and AMR-CSI algorithms are shown in Figures 4(c)-(h). As can be seen, the main improvement over the blind inversion is the enhanced retrieval of the quantitative real part of the bone. Other than this, the rest of the reconstruction does not show any significant improvements over blind inversion. Finally, we consider to use the *partial* and *wrong* SP shown in Figure 5(a). The SP is partial as it misses one bone region and it is wrong as it mistakenly assumes a square-shaped region (Region IV in Figure 5(a)). The MRSP-GNI, AMR-GNI and AMR-CSI reconstructions using these SP are shown in Figures 5(b)-(g). As can be seen, all of these algorithms are able to detect the presence of the second bone which was missing in the partial SP. Also, they have all alleviated the presence of the wrong spatial prior regarding the square-shaped region. Note that although the square-shaped region is still visible in the reconstructions, its quantitative value is similar to the muscle region as it should.

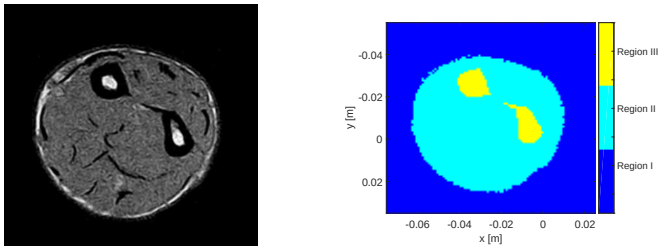

(a) MRI image (b) SP

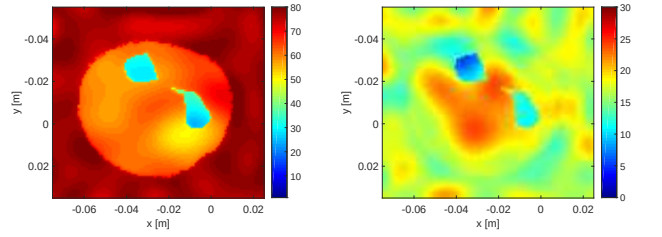

(c) $\mathrm{Re}(\epsilon_r)$, MRSP-GNI (d) $-\mathrm{Im}(\epsilon_r)$, MRSP-GNI

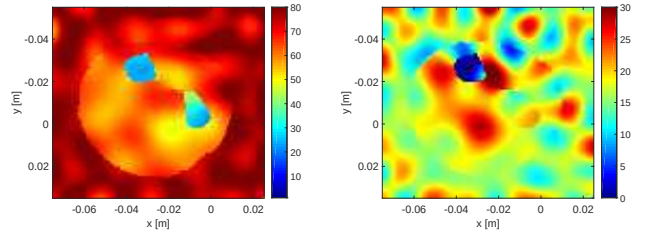

(e) $\mathrm{Re}(\epsilon_r)$, AMR-GNI (f) $-\mathrm{Im}(\epsilon_r)$, AMR-GNI

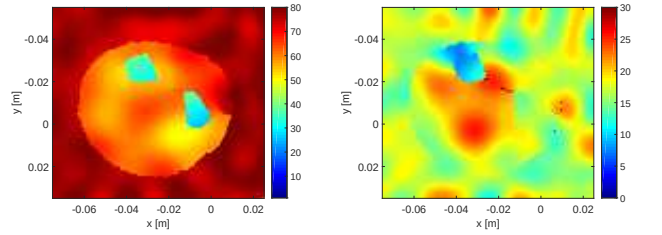

(g) $\mathrm{Re}(\epsilon_r)$, AMR-CSI (h) $-\mathrm{Im}(\epsilon_r)$, AMR-CSI

Fig. 4. (a) The MRI image of the forearm (This image was taken from [13], ©[2013] IEEE, and was also presented at [19]). (b) The SP derived from the MRI image. Real [left] and imaginary [right] parts of the reconstructed relative complex permittivity using the (c)-(d) MRSP-GNI algorithm, (e)-(f) AMR-GNI algorithm, and (g)-(h) AMR-CSI algorithm.

V. Conclusion

A simple and easy-to-implement approach to modify the existing microwave imaging algorithms employing MR was

[5]Note that these blind inversions can still be improved by balancing the real and imaginary parts of the unknown contrast in the inversion process; however, in that case, the balancing factor should be considered as a different type of prior information. Thus, the balanced inversion is not considered herein.

[6]Image registration needs to be performed so that we can use the MRI image for inversion. Herein, we have used a preliminary and *ad hoc* method to extract the SP from the MRI image. First, after applying some thresholding on the MRI image, its resolution was decreased using the MATLAB command *interpn* to make its discretization the same as that of the microwave inversion. Then, we have compared this post-processed MRI image with the blind reconstruction shown in Figure 3. Based on the visual inspection, we have performed some translational movements (i.e., movements along the $\hat{x}$ and $\hat{y}$ directions) on the post-processed MRI image to merely adjust its overall external contour with respect to that of the blind reconstructions. We have then used this translated post-processed MRI image as the SP.

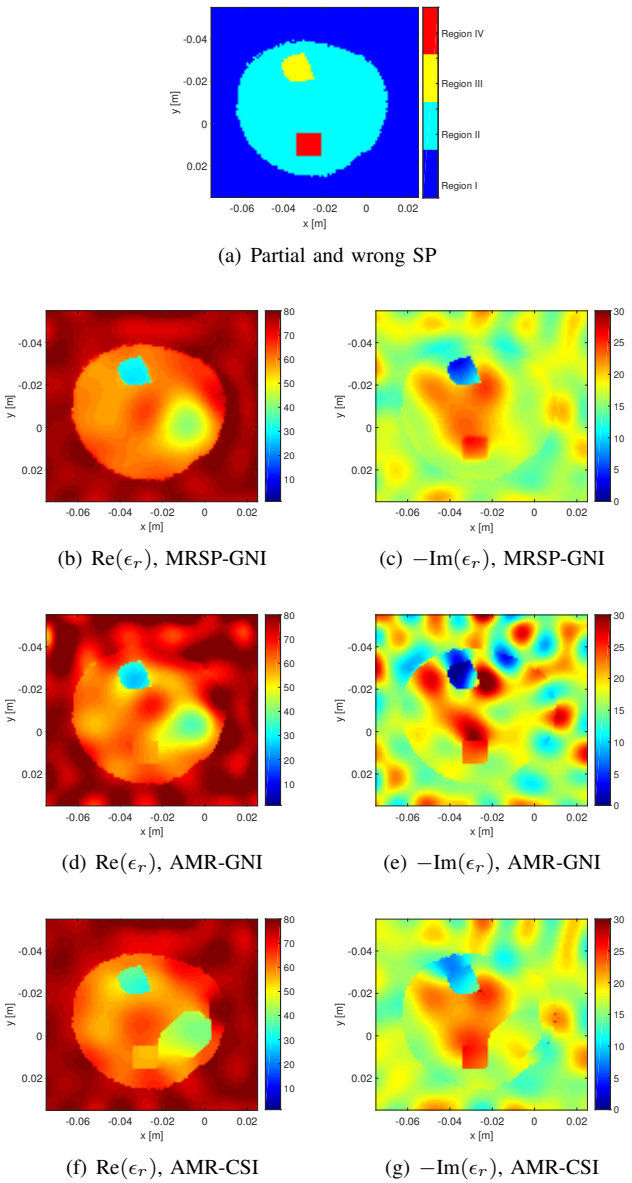

(a) Partial and wrong SP

(b) $\mathrm{Re}(\epsilon_r)$, MRSP-GNI

(c) $-\mathrm{Im}(\epsilon_r)$, MRSP-GNI

(d) $\mathrm{Re}(\epsilon_r)$, AMR-GNI

(e) $-\mathrm{Im}(\epsilon_r)$, AMR-GNI

(f) $\mathrm{Re}(\epsilon_r)$, AMR-CSI

(g) $-\mathrm{Im}(\epsilon_r)$, AMR-CSI

Fig. 5. (a) The incomplete (partial) and wrong SP which misses a bone region and mistakenly assume a square-shaped region. Real [left] and imaginary [right] parts of the reconstructed relative complex permittivity using the (b)-(c) MRSP-GNI algorithm, (d)-(e) AMR-GNI algorithm, and (f)-(g) AMR-CSI algorithm.

proposed to incorporate complete or partial available spatial priors into the inversion process. This method adds one extra term to the integrand of the standard multiplicative regularizer. Based on the results presented, the incorporation of spatial priors seems to enhance the quantitative accuracy achievable from microwave imaging.

Acknowledgment

We'd like to thank the Electromagnetic Imaging Laboratory at the University of Manitoba (Prof. Joe LoVetri) for letting us to use the forearm data set, and also the Institut Fresnel for providing the freely-available experimental data. We'd also like to thank Prof. Jean-Charles Bolomey for his suggestion regarding the use of the MRI image and the forearm data set.

References

[1] P. M. Meaney, A. H. Golnabi, N. R. Epstein, S. D. Geimer, M. W. Fanning, J. B. Weaver, and K. D. Paulsen, "Integration of microwave tomography with magnetic resonance for improved breast imaging," *Medical Physics*, vol. 40, no. 10, p. 103101, 2013.

[2] A. H. Golnabi, P. M. Meaney, and K. D. Paulsen, "Tomographic microwave imaging with incorporated prior spatial information," *IEEE Transactions on Microwave Theory and Techniques*, vol. 61, no. 5, pp. 2129–2136, May 2013.

[3] ——, "3D microwave tomography of the breast using prior anatomical information," *Medical Physics*, vol. 43, no. 4, pp. 1933–1944, 2016. [Online]. Available: https://aapm.onlinelibrary.wiley.com/doi/abs/10.1118/1.4944592

[4] A. H. Golnabi, P. M. Meaney, S. D. Geimer, and K. D. Paulsen, "3-D microwave tomography using the soft prior regularization technique: Evaluation in anatomically realistic MRI-derived numerical breast phantoms," *IEEE Transactions on Biomedical Engineering*, vol. 66, no. 9, pp. 2566–2575, Sep. 2019.

[5] L. M. Neira, B. D. V. Veen, and S. C. Hagness, "High-resolution microwave breast imaging using a 3-D inverse scattering algorithm with a variable-strength spatial prior constraint," *IEEE Transactions on Antennas and Propagation*, vol. 65, no. 11, pp. 6002–6014, Nov 2017.

[6] M. Omer, P. Mojabi, D. Kurrant, J. LoVetri, and E. Fear, "Proof-of-concept of the incorporation of ultrasound-derived structural information into microwave radar imaging," *IEEE Journal on Multiscale and Multiphysics Computational Techniques*, vol. 3, pp. 129–139, 2018.

[7] H. Jiang, C. Li, D. Pearlstone, and L. Fajardo, "Ultrasound-guided microwave imaging of breast cancer: tissue phantom and pilot clinical experiments," *Medical Physics*, vol. 32, no. 8, pp. 2528–2535, 2005.

[8] M. T. Bevacqua, R. Scapaticci, G. G. Bellizzi, T. Isernia, and L. Crocco, "Permittivity and conductivity estimation of biological scenarios via 3D microwave tomography," in *13th European Conference on Antennas and Propagation (EuCAP)*, March 2019, pp. 1–3.

[9] N. Abdollahi, D. Kurrant, P. Mojabi, M. Omer, E. Fear, and J. LoVetri, "Incorporation of ultrasonic prior information for improving quantitative microwave imaging of breast," *IEEE Journal on Multiscale and Multiphysics Computational Techniques*, vol. 4, pp. 98–110, 2019.

[10] N. Bayat and P. Mojabi, "Incorporating spatial priors in microwave imaging via multiplicative regularization," *IEEE Transactions on Antennas and Propagation (Available via IEEE Early Access)*, pp. 1–12, 2019.

[11] M. Bevacqua, G. Bellizzi, T. Isernia, and L. Crocco, "A method for effective permittivity and conductivity mapping of biological scenarios via segmented contrast source inversion," *Progress in Electromagnetic Research*, vol. 164, 2019.

[12] A. Abubakar, P. M. van den Berg, and J. J. Mallorqui, "Imaging of biomedical data using a multiplicative regularized contrast source inversion method," *IEEE Trans. Microwave Theory Tech.*, vol. 50, no. 7, pp. 1761–1777, July 2002.

[13] M. Ostadrahimi, P. Mojabi, A. Zakaria, J. LoVetri, and L. Shafai, "Enhancement of Gauss-Newton inversion method for biological tissue imaging," *IEEE Transactions on Microwave Theory and Techniques*, vol. 61, no. 9, pp. 3424–3434, Sept 2013.

[14] A. Abubakar, P. M. van den Berg, T. M. Habashy, and H. Braunisch, "A multiplicative regularization approach for deblurring problems," *IEEE Trans. Image Processing*, vol. 13, no. 11, pp. 1524–1532, Nov 2004.

[15] P. Mojabi and J. LoVetri, "Overview and classification of some regularization techniques for the Gauss-Newton inversion method applied to inverse scattering problems," *IEEE Transactions on Antennas and Propagation*, vol. 57, no. 9, pp. 2658–2665, Sept 2009.

[16] P. Mojabi, "Investigation and development of algorithms and techniques for microwave tomography," Ph.D. dissertation, University of Manitoba, Winnipeg, Manitoba, Canada, 2010.

[17] J.-M. Geffrin, P. Sabouroux, and C. Eyraud, "Free space experimental scattering database continuation: experimental set-up and measurement precision," *Inverse Probl.*, vol. 21, pp. S117–S130, 2005.

[18] P. Mojabi and N. Bayat, "A multiplicative regularizer to incorporate prior spatial data in microwave imaging reconstruction," in *European Conf. on Antennas and Propagation (EuCAP)*, March 2019, pp. 1–5.

[19] C. Gilmore, A. Zakaria, S. Pistorius, and J. LoVetri, "Microwave imaging of human forearms: Pilot study and image enhancement," *International Journal of Biomedical Imaging*, 2013.